Microwave radar cross sections and Doppler velocities measured in the surf zone

Gordon Farquharson[1] and Stephen J. Frasier

Microwave Remote Sensing Laboratory, University of Massachusetts, Amherst, Massachusetts, USA

Britt Raubenheimer and Steve Elgar

Woods Hole Oceanographic Institution, Woods Hole, Massachusetts, USA

[1] The relationship between microwave imaging radar measurements of fluid velocities in the surf zone and shoaling, breaking, and broken waves is studied with field observations. Normalized radar cross section (NRCS) and Doppler velocity are estimated from microwave measurements at near-grazing angles, and in situ fluid velocities are measured with acoustic Doppler velocimeters (ADVs). Joint histograms of radar cross section and Doppler velocity cluster into identifiable distributions. The NRCS values from pixels with large NRCS and high Doppler velocities (>2 m/s) decrease with decreasing bore height to the shoreline, similar to scattering from a cylinder with decreasing radius. The Doppler velocities associated with these regions in the histograms agree well with theoretical wave phase velocities. Radar and ADV measurements of fluid velocities between bore crests have similarly shaped energy density spectra for frequencies above about 0.1 Hz, but energy levels from the radar are an order of magnitude higher than those of the ADV data. Instantaneous interbore Doppler velocities are correlated with ADV measured fluid velocities but are offset by 0.8 m/s. This offset may be due to Bragg wave phase velocities, wind drift, range and azimuth sidelobes, the finite spatial resolution of the radar, and differences between mean flows measured at the surface with radar and flows measured below the surface with ADVs. Shoaling and breaking waves measured through radar grating lobes significantly affect both the Doppler velocities near the edges of the images and the scattering from the rear faces of waves, causing large Doppler velocities to be observed in these regions.

1. Introduction

[2] Measurement of nearshore processes traditionally is accomplished using fixed or drifting in situ devices. Pressure sensors are used to derive wave height, and electromagnetic current meters and acoustic Doppler velocimeters (ADVs) are used to measure subsurface velocity. However, large spatial coverage with sensor spacing fine enough to ensure measurement of small-scale nearshore processes, such as rip currents, leads to a prohibitively large number of in situ devices. Also, the deployment of these sensors tends to be difficult and time-consuming, and constant maintenance is required to remove debris, such as kelp, that collects on instrument mounting frames. Furthermore, sensors occasionally are buried as the bathymetry changes, contributing to the difficulties of long-term deployment. In situ sensors are also a hazard to swimmers and surfers, and injuries have occurred despite sufficient warning of instrument placement during experiments. To overcome some of these problems, other types of in situ instruments are used, such as drifters, which provide larger-scale Lagrangian measurements of currents. However, drifters require labor-intensive deployment and retrieval. Consequently, remote sensing techniques have been investigated as a means to provide large-scale measurements of nearshore processes.

[3] Optical, acoustic, and radar-based remote sensing techniques have been used to measure nearshore processes. Optical techniques have been used to provide estimates of the time-varying sandbar position [*Lippmann and Holman*, 1990], alongshore currents in the surf zone [*Chickadel et al.*, 2003], statistics of swash zone run-up [*Holman and Guza*, 1984; *Holman and Sallenger*, 1985; *Holland and Holman*, 1993], and bathymetry [*Dugan et al.*, 2001]. Processing of video images, such as tracking surface foam using particle image velocimetry derived algorithms, typically relies on visual contrast in the image, thus generally restricting optical techniques to the surf zone during daylight.

---

[1]Now at Earth Observing Laboratory, National Center for Atmospheric Research, Boulder, Colorado, USA.

[4] Doppler sonar has been used in the nearshore to measure acoustic intensity and Doppler velocities in rip currents [*Smith*, 1993; *Smith and Largier*, 1995]. The acoustic intensity is proportional to a combination of bubble density and suspended sediment, and Doppler velocity is the line of sight (radial) component of the scatterer velocity. However, acoustic measurements are limited by attenuation due to high densities of subsurface bubbles generated by breaking waves within the surf zone. Thus development of other techniques to measure velocities both inside and offshore of the surf zone is desirable.

[5] Microwave radar has proven to be useful in measuring oceanographic parameters, such as directional wave spectra [*Young et al.*, 1985; *Frasier et al.*, 1995], surface currents [*McGregor et al.*, 1997; *Moller et al.*, 1998], and nearshore bathymetric changes [*McGregor et al.*, 1998; *Trizna*, 2001]. However, radar has not been extensively applied to measuring surf zone currents. In this region, shoaling and breaking waves complicate the interpretation of Doppler velocities because different scattering mechanisms govern radar echos from broken and unbroken water surfaces. That is, Doppler velocities reflect the locally dominant scattering mechanism. This paper addresses the interpretation of microwave scattering within the surf zone.

[6] Microwave radar estimates of surf zone velocities have been compared with video-based estimates [*Puleo et al.*, 2003]. The results presented here extend previous studies by comparing radar with in situ current meters, allowing the radar to be ground truthed and, by investigating radar returns in more detail, allowing backscattering from shoreward propagating bores to be separated from backscattering from the water surface between bores.

[7] This paper starts with a brief overview of microwave radar scattering from the ocean surface in section 2. The field experiment and data collection are described in section 3, and the radar data processing is described in section 4. Estimates of normalized radar cross section (NRCS) and radar Doppler velocities and comparisons with in situ ADV-measured fluid velocities are presented in section 5. Radar image statistics are derived and used to characterize surf zone scattering. Doppler velocities associated with large NRCS features are compared with bore phase velocities, and interbore Doppler velocities are compared with in situ fluid velocities. Conclusions are presented in section 6.

2. Microwave Radar Scattering

[8] For vertical polarization at moderate incidence angles ($20°–70°$) and no wave breaking, microwave radar scattering from the ocean surface commonly is described by two-scale scattering from tilted, "slightly rough" surfaces [*Wright*, 1968; *Valenzuela*, 1968]. At X band frequencies, wind-generated gravity-capillary waves produce a slightly rough water surface. Larger-scale gravity waves are treated by dividing the surface into tilted facets that are locally slightly rough. In this formalism the radar cross section is determined primarily by the surface displacement spectrum evaluated at the Bragg resonant wavelength (approximately 1.5 cm for X band radar at near-grazing incidence angles).

The Doppler velocity measured by the radar is the power-weighted mean of the phase velocity of both the advancing and receding Bragg resonant waves (v_b) in a resolution cell plus any advection of the facet due to gravity wave orbital velocities (v_o), surface currents (v_c), and wind drift (v_w) [*Plant*, 1990].

[9] Composite surface theory and two-scale models do not describe the observed scattering from breaking waves on the ocean surface. Backscatter from breaking waves is observed to have large radar cross section values and Doppler velocities on the order of a few m/s [*Lewis and Olin*, 1980; *Keller et al.*, 1986; *Lee et al.*, 1995; *Liu et al.*, 1998; *Frasier et al.*, 1998]. Recent radar measurements of the surf zone region show significant backscatter for steepening waves, as well as for breaking waves and broken white water bores [*Puleo et al.*, 2003; *Haller and Lyzenga*, 2003]. Thus, for breaking waves, it is known that non-Bragg scattering mechanisms dominate over Bragg scattering at low grazing angles and that multiple scattering and multipath interference become increasingly important with increasing wave steepness and surface roughness [*Lee et al.*, 1999].
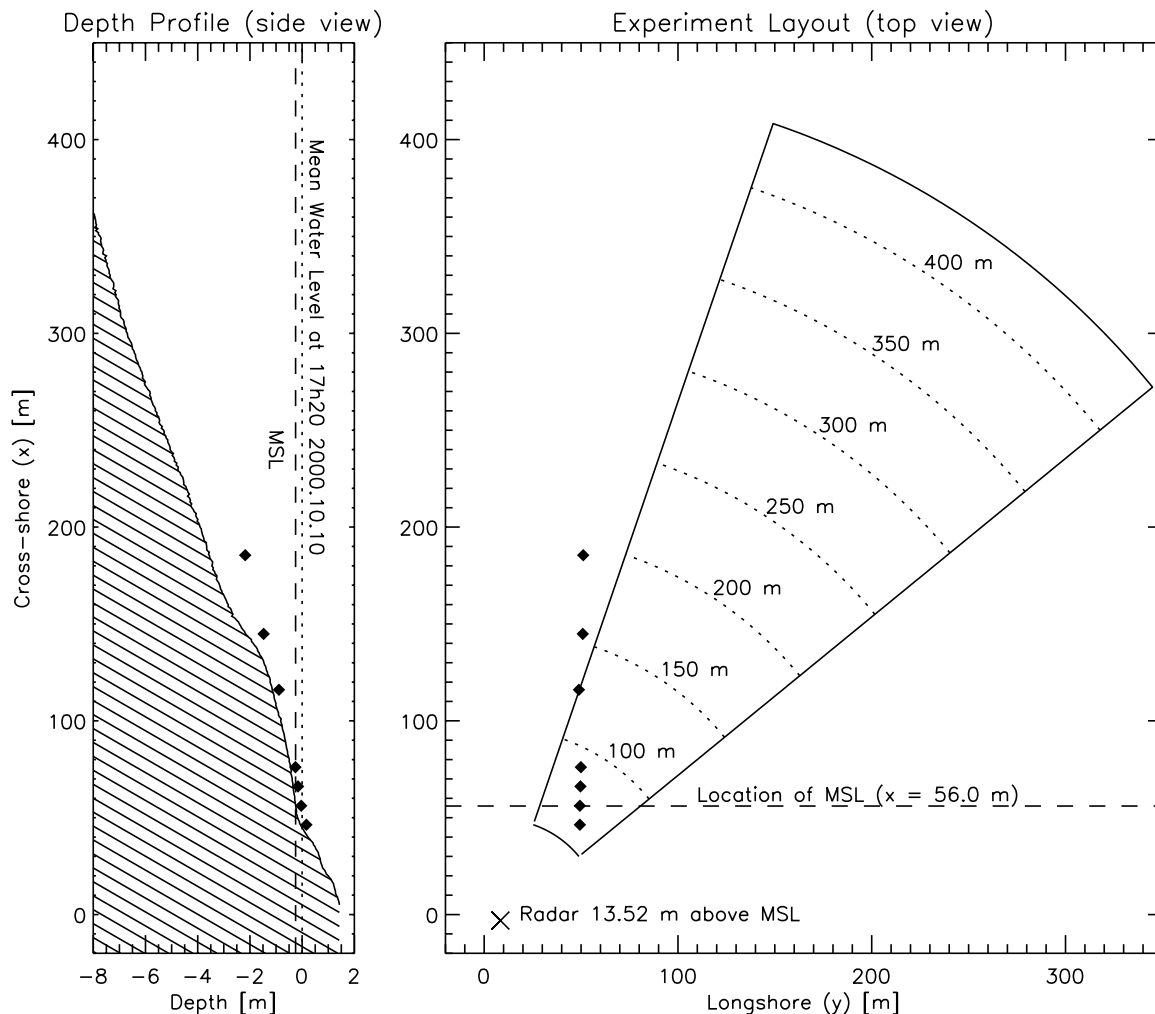
[10] Recent laboratory and field studies of scattering from breaking waves [e.g., *Sletten et al.*, 2003; *Puleo et al.*, 2003] confirm that observed Doppler velocities are consistent with the phase velocities of breaking waves. Thus radar cross sections for breaking waves in the surf zone are expected to be large compared with those for deep water nonbreaking waves, and surf zone Doppler velocities are expected to be on the order of wave phase velocities.

[11] The nearshore contains a variety of phenomena, including actively breaking waves in the breaker zone, white water bores in the surf zone, and unbroken water surfaces between wave crests, and thus a complex relationship exists between microwave backscatter and nearshore processes. This relationship is explored here by characterizing microwave scattering in the nearshore and relating the measurements to nearshore waves and fluid velocities.

3. Field Experiment

[12] Vertically polarized backscattered power and Doppler velocities were measured in the nearshore region at Scripps Beach, La Jolla, California [*Puleo et al.*, 2003] from 1700 to 1800 UT on 10 October 2000 using a second-generation Focused Phased Array Imaging Radar (FOPAIR) [*McIntosh et al.*, 1995]. FOPAIR is an X band microwave Doppler radar designed to image the sea surface with meter-scale resolution. The radar was deployed on the roof of a building 13.52 m above mean sea level (Figure 1). The imaging footprint of the radar system covered a $30°$ azimuthal sector with a resolution of $0.5°$ and a 384 m range with a resolution of 3 m. Radar images were recorded at a rate of 2.2 Hz over 20 min data runs.

[13] Simultaneously, a cross-shore transect of acoustic Doppler velocimeters and pressure sensors (Figure 1, diamonds) was used to measure subsurface fluid velocities and wave heights [*Raubenheimer*, 2002]. Data from the ADVs were recorded at 16 Hz for 3072 s (51.2 min) starting every hour. The distance from downward looking ADVs (located at cross-shore positions $x = 185, 144, 116, 66,$ and 56 m, Figure 1) to the seabed was measured every 3 s for 6.4 min

Depth Profile (side view)

Experiment Layout (top view)

Figure 1. (right) Layout of the experiment site showing the radar imaging area and the positions of the in situ instrument frames (diamonds). The radar was located 13.52 m above mean sea level on the southern corner of the roof of the Center for Coastal Studies building. Arcs (dotted curves) and associated distances indicate radial slant ranges from the radar. (left) The Scripps Beach cross-shore profile (depth relative to mean sea level) measured on 9 October 2000 at 1725 UT. Diamonds show the cross-shore and vertical positions of in situ measurement frames.

following each data run. Elevations above the sand of sideways looking ADVs (located at $x = 76$ and 46 m) were measured manually approximately hourly during daylight. Water depths (calculated from global positioning system surveys of sand levels and instrument locations combined with pressure measurements of the mean water level) at the shallowest and deepest sensors were 0.29 and 2.30 m, respectively.

[14] Offshore incident waves were measured in 5.78 m water depth at the end of the Scripps Pier at 1745 UT. The significant wave height was 1.22 m. The wave period and wavelength at the frequency of the primary power spectral peak were 5.22 s (0.192 Hz) and 32.4 m, respectively. A second peak in the wave spectrum at 11.6 s (0.086 Hz) corresponds to waves with a length of 86.5 m. The wind speed was 4.65 m/s from the west, almost directly onshore. Video observations show that the breaker zone was located near $x = 140$ m and bores from these breaking waves propagated through the surf zone toward the swash zone located at about $x = 50–60$ m.

4. Data Processing

4.1. Radar Image Processing

[15] The FOPAIR radar uses a frequency-modulated transmitted pulse to obtain fine range resolution with a medium-power coherent transmitter. To obtain azimuth resolution finer than the beamwidth of a single receive antenna, FOPAIR uses an array of receive antennas to detect backscatter and uses digital beamforming to form a focused radar image. The spacing between antenna elements is greater than one-half wavelength, yielding grating lobes that are located approximately ±32° in azimuth relative to the main beam. The grating lobes are suppressed, however, by the combined element patterns of the vertically polarized transmit and receive antennas.

[16]　The radar forms an image of the ocean surface in a period of approximately 0.64 ms, which is well within the decorrelation time for microwave backscatter at X band [*Plant et al.*, 1994]. A subsequent image is captured at τ = 1.5 ms later, and the covariance of the images $R(\tau)$ is computed for each pixel. The phase of $R(\tau)$ divided by $2\pi\tau$ has been shown to be an unbiased estimator of the first moment of the Doppler spectrum [*Miller and Rochwarger*, 1972], and thus

$$\bar{v}_{\mathrm{D}} = -\frac{\lambda}{2}\frac{\arg\{R(\tau)\}}{2\pi\tau} \qquad (1)$$

is an estimate of the mean Doppler velocity, where λ is the radar wavelength.

[17]　Backscattered power and velocity are time averaged to produce a processed data image rate of 2.2 Hz. For a pulse pair spacing of 1.5 ms the unambiguous Doppler velocity range is ±5 m/s. Doppler velocities from advancing breaking waves occasionally exceed the maximum unambiguous velocity. For this work, these velocities are unwrapped by adding observed (aliased) velocity values less than −2 to 10 m/s. NRCS (σ^0) values are estimated from mean backscattered power measurements using nominal system parameters.

[18]　For each pixel in the radar image the minimum radar cross section is estimated from the measured noise figure of the receiver and an assumed operating temperature. The minimum NRCS detectable by the radar along the center beam ranges from below −50 dB along the boresight direction for near ranges to −36 dB at far ranges. At the edges of the image, sensitivity decreases and the minimum NRCS is between −40 and −20 dB. Typical NRCS values measured at grazing angles of around 1° with low to moderate wind speeds are around −40 dB [*Wetzel*, 1990]. Thus it is expected that near the edges of the images, pixels will contain NRCS values that are less than the minimum detectable NRCS. The processing code marks such pixels as missing data.

4.2.　Radar and in Situ Time Series Processing

[19]　To compare radar with ADV time series, radar time series were interpolated to the 16 Hz sampling rate of the ADVs. Both time series were then low−pass filtered with a cutoff frequency of 1 Hz and decimated to a sampling rate of 2 Hz. This procedure ensures that the filter has the same effect on both Doppler and current meter time series.

[20]　Subsurface velocities (v_{hs}^i) are converted to surface velocities (v_0^i) using linear wave theory [*Guza and Thornton*, 1980] in which

$$v_0^i = \frac{\cosh(kh)}{\cosh(k(h-h_s))}v_{h_s}^i, \qquad (2)$$

where k is the wave number of the ocean waves, h is the water depth, h_s is the distance above the bottom of the subsurface sensor, and the superscript i indicates the cross-shore and alongshore components of horizontal velocity. The correction was applied at wind wave frequencies (0.005 Hz $\leq f \leq$ 0.300 Hz) for all the in situ velocities presented here.

[21]　The radial component of the surface velocity is computed using

$$v_{\mathrm{radial}} = u_0\sin(\phi) - v_0\cos(\phi), \qquad (3)$$

where u_0 is the cross-shore velocity, v_0 is the alongshore velocity, and ϕ is the angle from the radar to the sensor measured from the positive alongshore direction.

5.　Results and Analysis
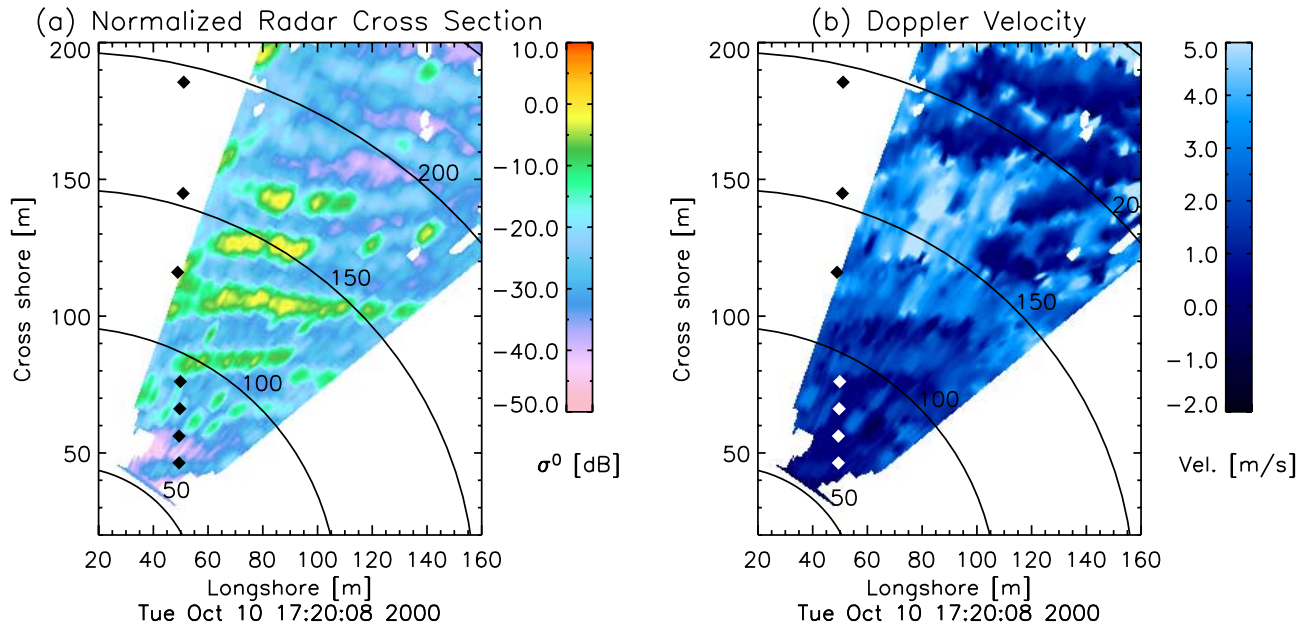
5.1.　Radar Images

[22]　Images of normalized radar cross section and associated Doppler velocity georeferenced to the experiment coordinate system (Figure 2) show that NRCS (σ^0) values range from −50 to around 0 dB. NRCS signatures of breaking wave crests in the surf zone (70 m $\leq x \leq$ 140 m) are above −10 dB and are mostly parallel to the shore. NRCS values between these bright features are around −30 dB. Some evidence of backscattered power measured through grating lobes is seen on the left-hand side of the image at x = 110−130, 160, and 200 m, where scattering from bright features appears to wrap around from the right-hand side of the image and to continue on the left at the same radial range.

[23]　Unwrapped radar Doppler velocities range from −2 to 5 m/s. Positive Doppler velocities represent motion toward the radar. Individual Doppler velocity wave signatures, especially between radial ranges from 120 to 170 m, are less distinct than those in the NRCS image.

5.2.　NRCS and Doppler Velocity Distributions

[24]　Breaking wave fronts result in large radar cross sections (Figure 2, yellow bands), with Doppler velocities on the order of the phase velocity of the wave. In contrast, interbore radar cross sections (Figure 2, blue areas) are more similar to offshore NRCS values, suggesting Bragg-dominated scattering in which Doppler velocities are a combination of water particle orbital velocity, Bragg wave phase velocity, and surface currents. Each of these processes can be identified by its distinct distribution of NRCS and radar Doppler velocities.

[25]　To mitigate the effect of grating lobes, which affect Doppler velocities near the edges of the radar images, joint histograms of NRCS and Doppler velocities (Figure 3) were computed using only the central radar beams between −2.49° and +2.49° and between radial ranges from 72 to 192 m. For these beam angles the grating lobe suppression is greater than 43 dB. All regions show peaks in the histograms at σ^0 near −30 dB and velocities near 0.5 m/s. A secondary peak with $\sigma^0 > -20$ dB and velocity >2 m/s also exists for all regions. The sources of these peaks will be discussed in sections 5.3 and 5.4. The near-zero velocity peak in region 1 is due to scattering from the stationary instrument frames on which the in situ sensors were mounted. In regions 5−8, another peak occurs at $\sigma^0 < -30$ dB and velocity >2 m/s. Backscatter in this distribution is due to scattering from shoaling and breaking waves measured through the radar grating lobes, and thus NRCS values in this distribution are not representative of the true NRCS because they are converted from backscattered power to NRCS using the main beam antenna gain. Al-

Figure 2. Focused Phased Array Imaging Radar (FOPAIR) images of (a) normalized radar cross section (NRCS) and (b) radar Doppler velocity georeferenced to the experiment coordinate system. Pixels below the system noise have been set to the background color (white). Arcs show the radial distance from the radar, and diamonds show the locations of the in situ instrument frames.

though scattering through the grating lobes is attenuated, it is strong enough to be observed in the central beams because the left-hand grating lobe is pointed almost directly into the breaking waves and thus has a much higher NRCS than the obliquely pointed main beam. Grating lobe scattering significantly affects radar Doppler velocities near the edges of the images and also scattering from the back faces of waves where NRCS values are low.

5.3. Nearshore Breaking Waves and Surf Zone Bores

[26] The peak, mean, and standard deviation of the velocity distribution conditioned on NRCS values above −20 dB (i.e., the secondary peaks) are given for each subregion in Table 1. The mean velocities decrease from 4.79 to 1.62 m/s with decreasing range (depth).

[27] Assuming that ocean wavelengths are much longer than the water depth and that surf zone wave heights are a constant fraction of the water depth (depth-limited waves) [*Suhayda and Pettigrew*, 1977; *Thornton and Guza*, 1982; *Raubenheimer et al.*, 1996], wave phase velocities C_p are given by

$$C_p = \sqrt{(1+\gamma)gh}, \tag{4}$$

where g is gravitational acceleration and γ is the ratio of significant wave height to water depth. Estimating the radial component of the wave phase velocity as
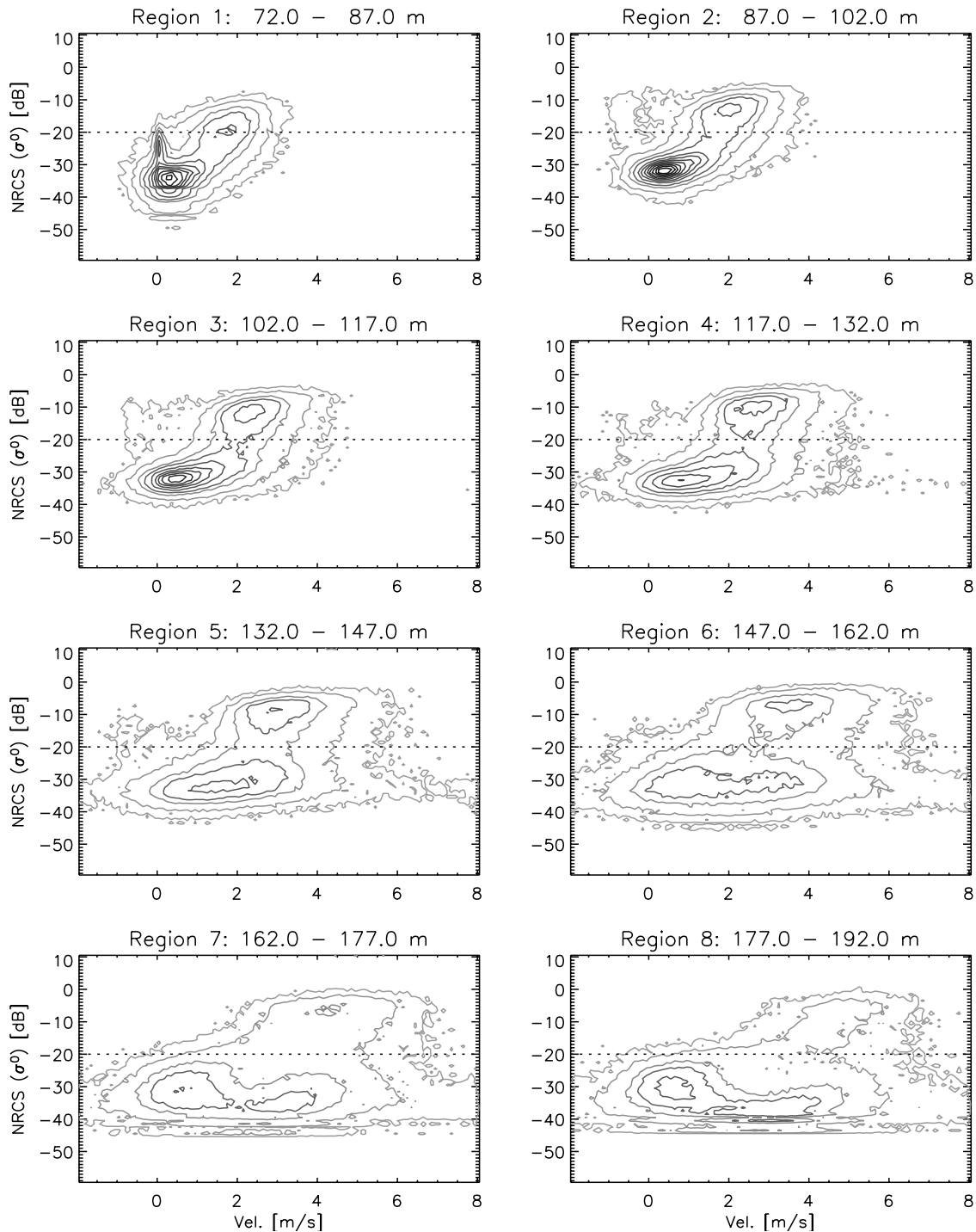
$$C_p = \sqrt{(1+\gamma)gh}\, cos(\phi)$$

and using $\gamma = 0.43$ [*Raubenheimer*, 2002], wave phase velocities in the eight subregions are shown to agree well with the velocities in the secondary NRCS peaks (Figure 4). The agreement between the predicted and observed velocities (RMS difference is 0.17 m/s) suggests that pixels

with large NRCS and Doppler velocities result from broken wave bores propagating through the surf zone.

[28] Although the means of the distributions (Figure 3) associated with the secondary peaks agree well with the predicted phase velocities (Figure 4), pixels with the largest NRCS have higher Doppler velocity values (Figure 3) than predictions. Thus mean Doppler velocities of surf zone bores estimated from the largest individual values of NRCS (Figure 4, squares) (see also *Puleo et al.* [2003, Figure 9c], who use the same data used here) rather than those estimated from the peak of the distribution (i.e., the highest-valued contours in Figure 3) as used here are significantly larger than predicted velocities (Figure 4). The physical mechanism associated with these largest velocities remains uncertain. Measurements of breaking waves in a laboratory wave channel show that particle velocities near the crest are approximately equal to or greater than the wave phase velocity [*Komar*, 1998]. Possibly, the largest radar Doppler velocities result from velocities at the crests of the observed plunging waves that exceed the phase velocity as the waves become unstable and begin to break.

[29] Although the bore NRCS values decrease from about −5 ($x = 140$ m) to −19 dB ($x = 60$ m) as the waves approach the swash zone (Figure 5), the interbore NRCS values are roughly constant (−32 ± 2 dB) (Figure 3). Thus the decrease in bore NRCS values is unlikely to be caused by errors associated with compensating for the gain pattern of the antennas. Instead, the correspondence between the maximum bore NRCS value and the location of wave breaking ($x = 140$ m) suggests that the bore NRCS is related to the wave height. Following studies for plumes, which are similar in shape to surf zone bores, albeit much smaller, backscatter from the bore front faces that are much larger in height than the radar wavelength is calculated from

Figure 3. Contour plots of joint histograms of NRCS and Doppler velocity for radar beams from −2.49° to +2.49°. The NRCS bin size is 1 dB, and the Doppler velocity bin size is 0.1 m/s. The radial distance from the radar is listed above each panel.

the physical optics approximation for scattering from a smooth cylinder [*Wetzel*, 1990]

$$0.5k_e a L^2, \qquad (5)$$

where k_e is the radar wave number, a is the wave height estimated as γh, and L is the length of the cylinder, which is equal to the width of the radar pixel. Comparison of observed bore NRCS values with values predicted using

equation (5) and $\gamma = 0.43$ (Figure 5) shows that the trend of decreasing bore NRCS with decreasing depth is predicted well. The predicted bore NRCS values are 3–4 dB larger than the observed values for all cross-shore locations except at the most shoreward and most seaward points, where the significant wave heights are expected to diverge from a linear trend [*Raubenheimer*, 2002, Figure 4]. Thus the observed onshore decrease in bore NRCS appears to be related to the decrease in surf zone

Table 1. Joint Probability Distribution Statistics for Pixels With NRCS Values Greater Than −20 dB[a]

Region, m	Peak σ^0, dB	Peak Velocity, m/s	Mean Velocity, m/s	Velocity SD, m/s
72–87	−19	1.80	1.62	0.55
87–102	−14	1.90	1.94	0.57
102–117	−12	2.20	2.29	0.57
117–132	−11	2.40	2.64	0.58
132–147	−9	2.90	3.06	0.71
147–162	−8	3.70	3.54	0.85
162–177	−6	4.10	4.38	0.88
177–192	−7	4.40	4.79	0.79

[a]Values are computed using only the central radar beams between −2.5° and +2.5°. "Region" refers to the radial distance from the radar, σ^0 is the NRCS, and SD is standard deviation.

wave height. Using half the wave height for a would give an almost perfect agreement.

[30] The physical optics approximation (equation (5)) neglects multipath scattering between the water in front of the bore and the bore, which can affect the NRCS of any given bore. When averaging over a long time series with many different sized bores, these effects (which are sensitive to the position of the scatterers on the bore [*Wetzel*, 1990]) tend to cancel, and thus equation (5) remains a reasonable approximation.
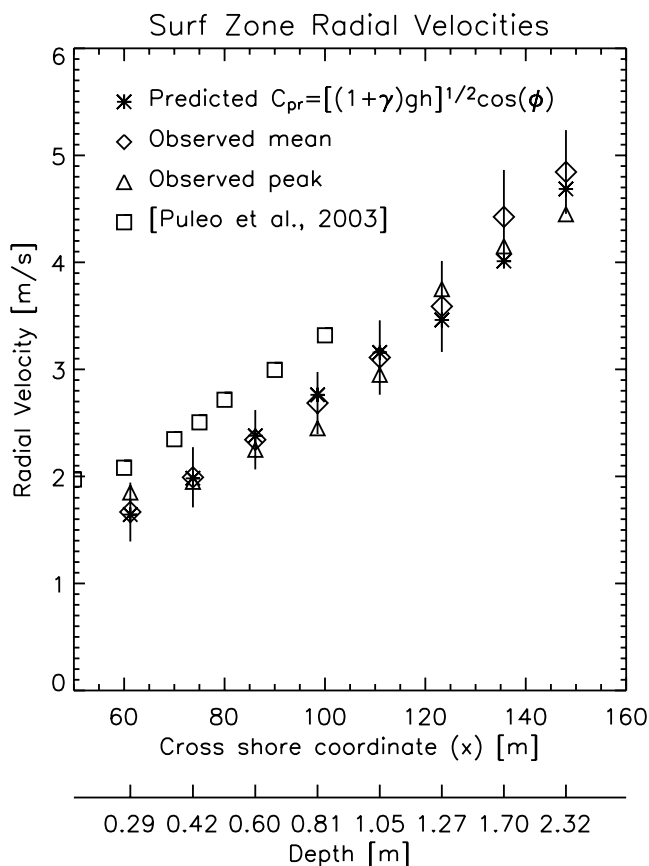
5.4. Time Series Analysis of Radar Doppler and ADV Velocities

[31] A time series of radar Doppler velocities was extracted from the pixel at x = 76.6 and y = 52.3 m, approximately 3 m from the fourth ADV from shore. The location of this pixel avoids corruption of radar measurements caused by backscatter from the instrument frame. The ADV was located 0.05 m above the bed, and the nominal water depth was 0.5 m. Wave signatures in the radar Doppler velocity time series are aligned with the nearby ADV radial wave orbital velocities (Figure 6). Large differences exist for wave crest signatures (positive ADV velocity) because the radar measures the phase velocity of the bore, whereas the ADV measures the wave orbital velocity. Between the bores, there is a significant offset between the radar and ADV velocities, which is discussed below.
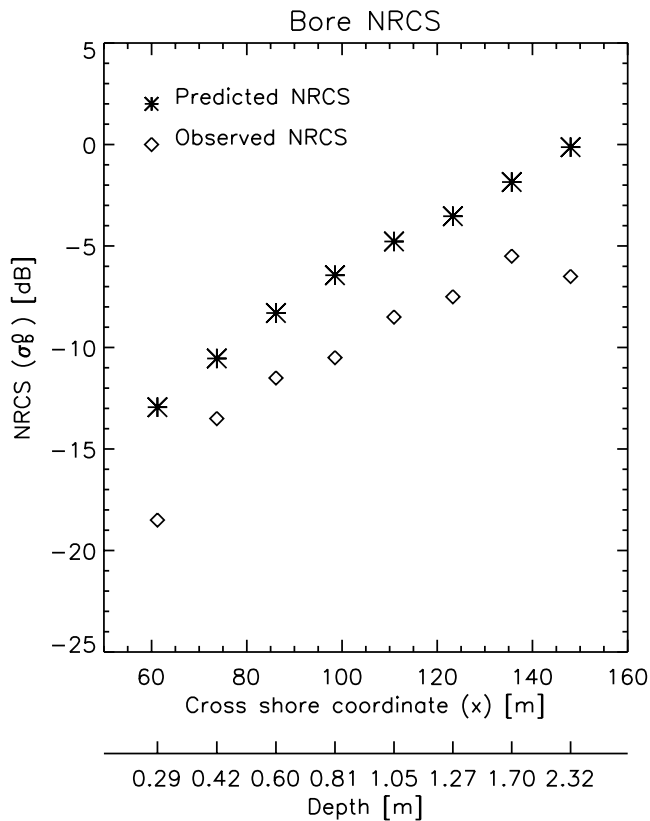
[32] Spectra were estimated from both radar and ADV radial velocity time series (Figure 7). In contrast to the radar velocity spectrum, which has a primary peak at 0.08 Hz (12.5 s), the ADV spectrum has no significant peaks in the swell frequency band (0.05 Hz $\leq f \leq$ 0.15 Hz). Furthermore, at 0.08 Hz the ADV-measured velocity energy density is about 10 times smaller than the radar-measured velocity energy density (Figure 7a), and the radar velocity fluctuations lead the ADV velocity fluctuations by about 30° (Figure 7c). Likely, the large bore phase velocities measured by the radar are responsible for the difference between the radar and ADV velocity spectral levels. The similar spectral shapes (Figure 7a) (including the $\sim f^{-8/3}$ roll-off above 0.3 Hz) and the high squared coherence (greater than 0.4 for $f \leq$ 0.20 Hz, Figure 7b) suggest that Doppler and ADV velocities in the interbore region (where turbulence may have a surface signature) are consistent with each other.

[33] To investigate interbore velocities further, a joint histogram of NRCS and Doppler velocity was computed from the time series at x = 76.6 and y = 52.3 m (Figure 8a). Similar to the subregional histograms in section 5.3 (Figure 3), the joint histogram for the pixel shows peaks at low (−32 dB) and high (−14 dB) NRCS (Figure 8a). Radar velocities with low NRCS values (−40 to −25 dB), corresponding to interbore scattering, agree with ADV velocities (Figure 8b, correlation coefficient

Figure 4. Radial velocity versus cross-shore coordinate (and depth). Asterisks are theoretically predicted shallow water phase velocities (equation (4)), diamonds are observed radial velocities corresponding to the means of the joint histograms for radar beams from −2.49° to +2.49°, triangles are the observed radial velocities corresponding to the peaks of the histograms, and squares are the observed radial velocities corresponding to pixels with the largest NRCS values [from *Puleo et al.*, 2003]. The RMS difference between the observations (diamonds) and the predictions (asterisks) is 0.17 m/s.

Figure 5. Predicted (asterisks) (equation (5)) and observed (diamonds) NRCS values versus cross-shore coordinate (and depth). Corresponding interbore NRCS values are −32 ± 2 dB.
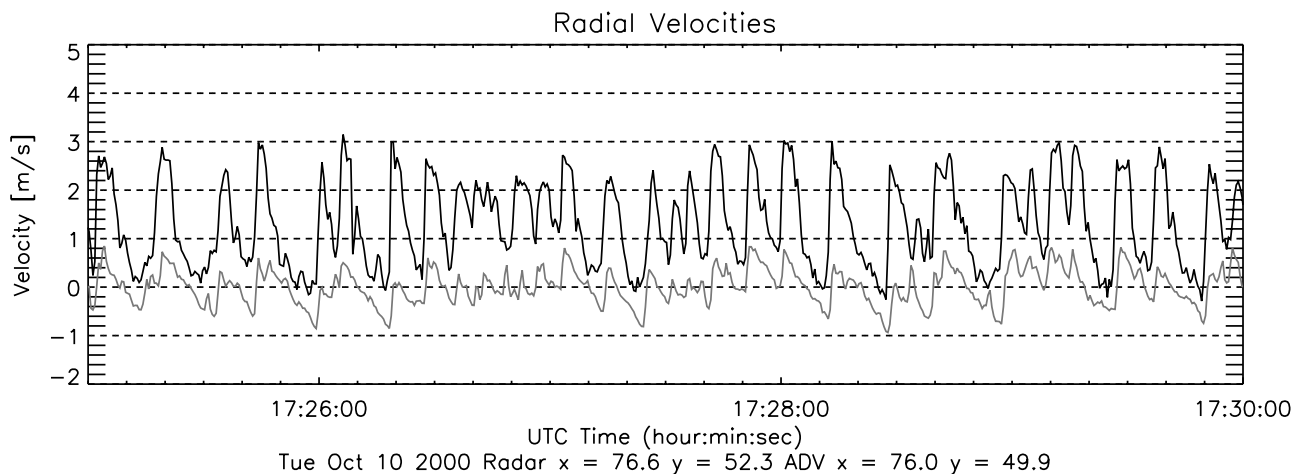
$r^2 = 0.43$) except for an offset of about 0.81 m/s (e.g., the mean velocities are 0.67 m/s for the radar and −0.14 m/s for the ADV). The agreement between the radar and ADV interbore velocities supports the assertion that differences

in spectral levels between radar and ADV velocities are primarily due to the large bore phase velocities.

[34] The offset between radar and in situ velocities can be attributed to one or more factors, including both instrument limitations and fundamental differences in the currents observed near the surface and near the bottom. The most significant instrument limitation is the influence of range and azimuth sidelobes from large NRCS breaking waves for which the Doppler velocity is representative of the phase velocity of the wave (C_p). Doppler velocities from such intense echoes may contaminate the velocities reported between the bores. Interbore radar-measured Doppler velocities are the power-weighted sum of bore and interbore velocities. Using a simple model for this effect, the adjusted Doppler velocity, equal to the wave orbital velocity (v_o) plus the surface current (v_c), is given by
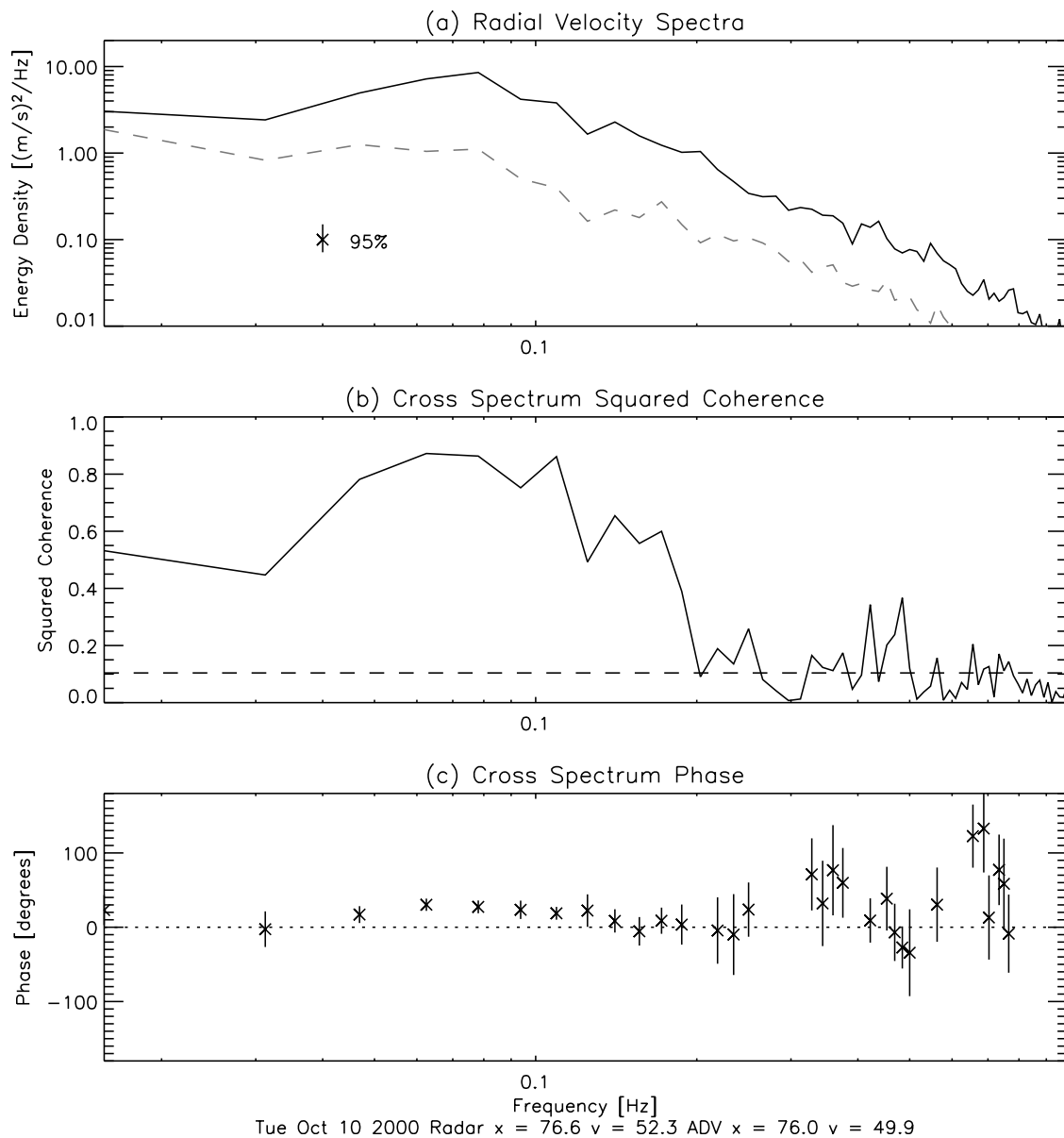
$$(v_o + v_c) = \frac{S_1 + P_2}{P_2} v_d - \frac{S_1}{P_2} C_p - (v_w + v_b), \quad (6)$$

where the sidelobe power S_1 is approximated as the peak NRCS for breaking waves (~−14 dB in Figure 8a) minus the estimated range gate leakage (~−28 dB), the peak NRCS P_2 is estimated as the peak value in a given NRCS range, C_p is the mean phase velocity for the breaking waves (~2.19 m/s), and the radar-measured Doppler velocity v_d is based on the velocity of each data point. Using nominal values for the Bragg resonant wave phase velocity $v_b = 0.23$ m/s and for the radial wind drift $v_w = 0.11$ m/s (where drift is estimated as 3% of the 10 m wind speed of 4.65 m/s), the adjusted Doppler velocity is computed for two NRCS ranges (−34 dB ≤ σ^0 < −30 dB and −30 dB ≤ σ^0 < −26 dB). After correcting for the sidelobe effects, the adjusted mean ($v_o + v_c$) radar radial velocity and the mean ADV radial velocity for the lower (−34 dB ≤ σ^0 < −30 dB, Figure 9a) NRCS conditional distributions are −0.06 and −0.23 m/s, respectively, and the adjusted mean radar radial velocity and the mean ADV radial velocities for the upper (−30 dB ≤ σ^0 < −26 dB, Figure 9b) NRCS conditional

Figure 6. Velocity versus time on 10 October 2000 between 1725 and 1730 UT. The solid curve is radar Doppler velocity at $x = 76.6$ m, $y = 52.3$ m, and the shaded curve is acoustic Doppler velocimeters (ADV) radial velocity at $x = 76.0$ m, $y = 49.9$ m. The approximately 3 m separation between the pixel used for the radar Doppler velocity and the ADV frame is sufficient to prevent interference with the radar measurements. The data have been processed to a 2 Hz sample rate.
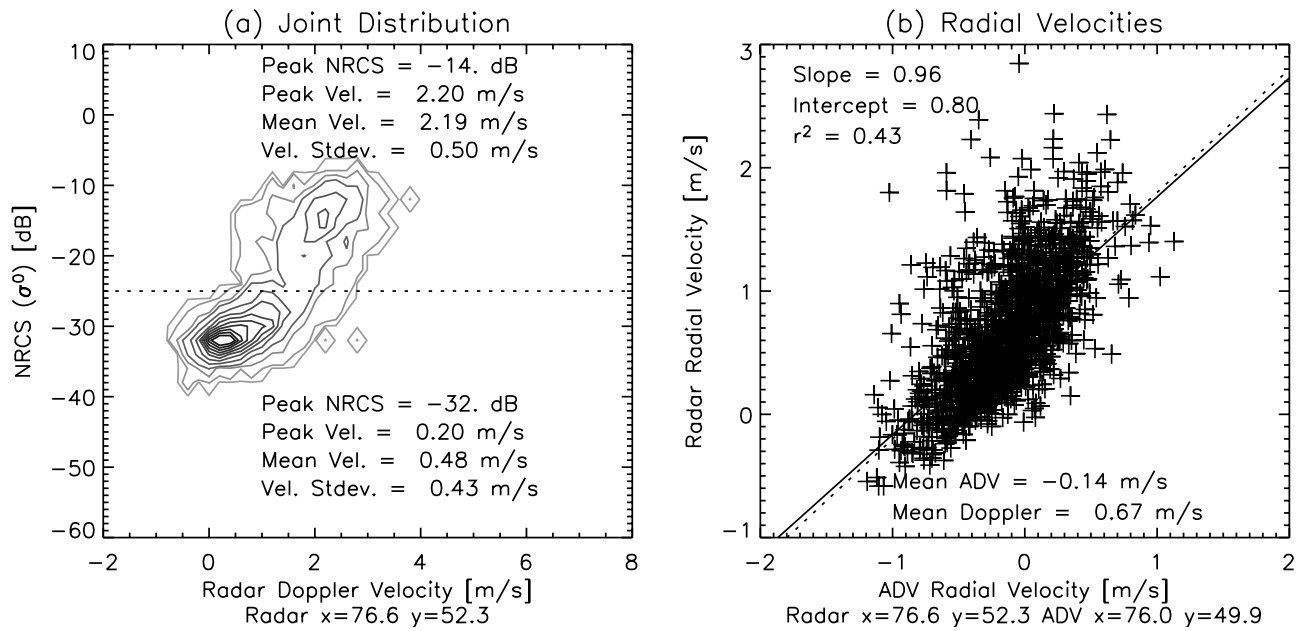
Figure 7. (a) Energy density of Doppler (solid curve) and ADV radial (shaded dashed curve) velocity, (b) squared coherence, and (c) phase between Doppler and ADV velocity versus frequency for 20 min time series. The 95% confidence limits on spectral estimates (0.04 Hz frequency resolution) are shown in Figure 7a, the 95% significance level for zero coherence is shown as a dashed horizontal line in Figure 7b, and the 95% confidence ranges on the phase estimates are shown as vertical bars through each symbol in Figure 7c. Phase estimates are shown only for squared coherence values that are larger than the 95% significance level.
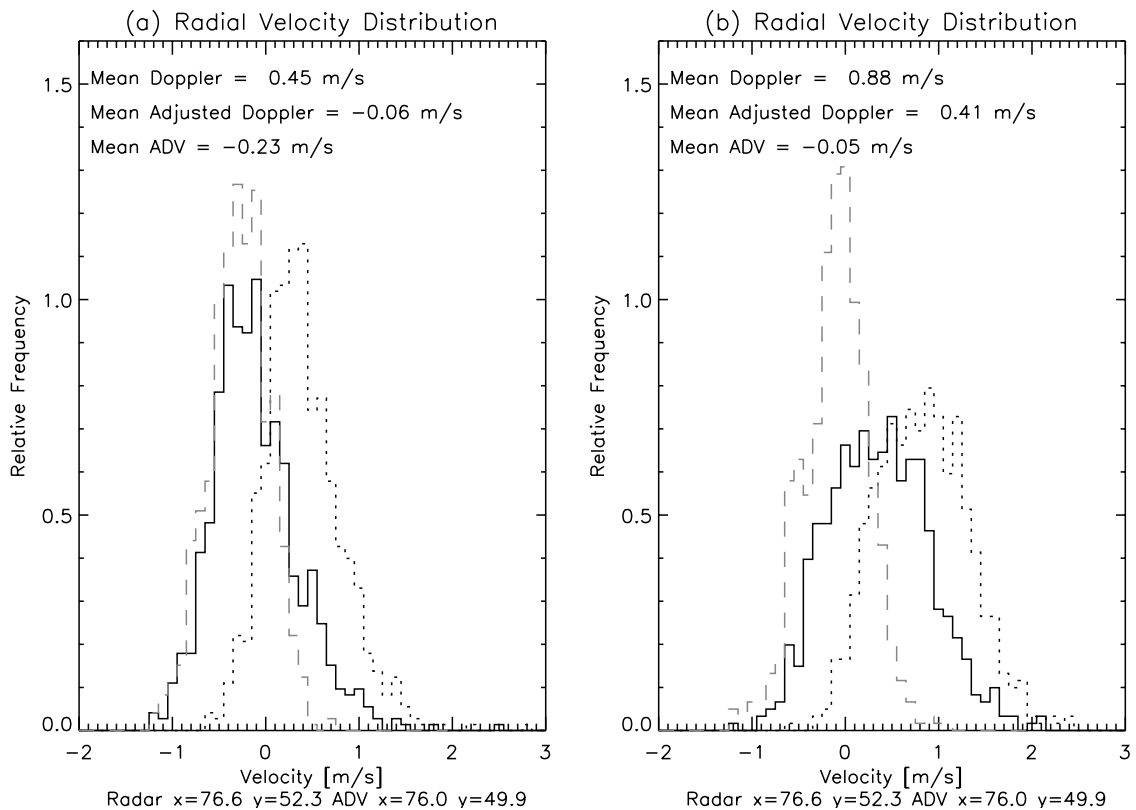
distributions are 0.41 and −0.05 m/s, respectively. Thus, although the radar velocity distribution is broader than the ADV distribution, the differences between the adjusted mean radar and mean ADV velocities have been reduced to 0.17 m/s for the lower distribution and and 0.46 m/s for the upper distribution.

[35] Correlation of amplitude and frequency modulations of the Bragg scatterers [*Keller and Wright*, 1975] also may contribute to the offset. At near-grazing angles, coherent pulse pair averages of 0.25 s are biased by up to 0.20 m/s for upwind and up-wave conditions, compared with inco-herent pulse pair averages [*Moller et al.*, 1998]. Reprocess-ing the radar data using incoherent pulse pair averaging does not change the mean adjusted Doppler velocity for the lower NRCS range but reduces it from 0.41 to 0.34 m/s for the upper NRCS range. Therefore some of the remaining difference in radar and ADV mean velocity may be due to the simplicity of the range and azimuth sidelobe model used. Using a sidelobe level of −26 dB (2 dB less than that used above) so that $S_1 = -40$ dB reduces deviations between mean radar and ADV velocities to 0.05 m/s for the lower NRCS range and 0.25 m/s for the upper NRCS

Figure 8. (a) Contour plot of joint histograms of NRCS and Doppler velocity for the time series shown in Figure 7 (x = 76.6 m, y = 52.3 m). The NRCS bin size is 2 dB, and the Doppler velocity bin size is 0.2 m/s. (b) Radar Doppler velocity versus ADV radial velocity. Doppler velocities were selected from pixels with NRCS value between −40 dB and −25 dB. The solid line shows the least squares fit for the data, and the dotted line is a 1:1 relationship with an 0.81 m/s offset.

Figure 9. Conditional distribution of radial velocity time series at x = 76.6 m, y = 52.3 m for (a) −34 σ^0 ≤ −30 dB and (b) −30 σ^0 ≤ −26 dB. The dotted and solid curves show the distribution before (v_d) and after ($v_o + v_c$) compensating for sidelobes, and the dashed curves show the distribution of the ADV radial velocities for each NRCS range.

range. Thus the adjustment is sensitive to the sidelobe level used, illustrating the need for low range and azimuth sidelobe levels for nearshore radar measurements.

[36] Another expected but potentially significant source of differences between radar and in situ estimates of velocity is vertical shear in offshore-directed mean currents (undertow). The ADVs measured velocity between about 0.05 and 0.50 m above the sea floor, where flows may differ from those near the surface. For example, during the field deployment an approximately 0.15 m/s offset was observed between the offshore-directed flows measured with the ADVs and flows estimated with surface drifters in the surf zone [*Schmidt et al.*, 2003].

[37] Last, finite radar range resolution may also contribute to differences between radar and ADV velocities. The interbore velocity measured by the ADV has been assumed to be due only to the orbital velocities of the waves at the peak wave period (11.50 s). However, the offshore wave field has an additional peak in the wave spectrum at 5.22 s, which corresponds to a wavelength of only 11.4 m at $x = 76.6$ m (water depth = 0.5 m). In contrast to the radar velocity spectrum, the ADV velocity spectrum shows a weak peak at this frequency (Figure 7). Although the 3 m resolution of the radar is able to resolve these short waves crudely, the radar-measured orbital velocities will be power weighted and spatially averaged. Backscattered power is larger for the front faces of the waves, and thus the power-weighted, spatially averaged velocity will be biased toward velocities approaching the radar, and the high-frequency waves may contribute to both the decorrelation and the offset seen in the scatterplot (Figure 8b).

6. Conclusions

[38] Surf zone scattering of microwave radar was analyzed using joint histograms of NRCS and Doppler velocities that are measured for each pixel in the radar images. Mean Doppler velocities from pixels with high NRCS were shown to agree well with a shallow water model for bore phase velocities in the surf zone, confirming observations made in previous studies. Furthermore, the observed decrease of NRCS values with decreasing water depth was shown to be similar to predictions of scattering from a cylinder with radius equal to the significant wave height, which also decreases with decreasing depth. Thus, for high NRCS, microwave backscatter is dominated by scattering from breaking waves and subsequent bores, and the associated Doppler velocities are dominated by the phase velocity of these waves.

[39] Instantaneous mean Doppler velocities with low NRCS (interbore velocities) were well correlated with in situ ADV observations of velocities, spectral shapes of radar and ADV velocities were similar for swell frequencies, and radar spectral energy roll-offs were similar to those from the ADVs for frequencies greater than about 0.3 Hz. The 0.81 m/s offset between radar and ADV interbore velocities can be explained by the effects of range and azimuth sidelobes and the phase velocity of Bragg resonant waves and surface wind drift, coherence between amplitude and frequency modulations of the scattering, the presence of high-frequency waves with wavelengths on the order of the radar resolution, and vertical shear of offshore-directed

mean currents. Within the shoreward region of the surf zone, radar estimates of interbore velocities are similar to surface velocities obtained by depth-correcting observations from near bottom in situ current meters, suggesting that radar can be used to measure surface currents and bore speeds in the surf zone.

References

Chickadel, C. C., R. A. Holman, and M. H. Freilich (2003), An optical technique for the measurement of longshore currents, *J. Geophys. Res.*, *108*(C11), 3364, doi:10.1029/2003JC001774.

Dugan, J. P., C. C. Piotrowski, and J. Z. Williams (2001), Water depth and surface current retrievals from airborne optical measurements of surface gravity wave dispersion, *J. Geophys. Res.*, *106*, 16,903–16,915.

Frasier, S. J., Y. Liu, D. Moller, R. E. McIntosh, and C. Long (1995), Directional ocean wave measurements in a coastal setting using a focused array imaging radar, *IEEE Trans. Geosci. Remote Sens.*, *33*(2), 428–440.

Frasier, S. J., Y. Liu, and R. E. Mcintosh (1998), Space-time properties of radar sea spikes and their relation to wind and wave conditions, *J. Geophys. Res.*, *103*, 18,745–18,757.

Guza, R. T., and E. B. Thornton (1980), Local and shoaled comparisons of sea surface elevations, pressures, and velocities, *J. Geophys. Res.*, *85*, 1524–1530.

Haller, M. C., and D. R. Lyzenga (2003), Comparison of radar and video observations of shallow water breaking waves, *IEEE Trans. Geosci. Remote Sens.*, *41*(4), 832–844, doi:10.1109/TGRS.2003.810695.

Holland, K. T., and R. A. Holman (1993), The statistical distribution of swash maxima on natural beaches, *J. Geophys. Res.*, *98*, 10,271–10,278.

Holman, R. A., and R. T. Guza (1984), Measuring run-up on a natural beach, *Coastal Eng.*, *8*, 129–140.

Holman, R. A., and A. H. Sallenger (1985), Setup and swash on a natural beach, *J. Geophys. Res.*, *90*, 945–953.

Keller, W. C., and J. W. Wright (1975), Microwave scattering and the straining of wind-generated waves, *Radio Sci.*, *10*, 139–147.

Keller, W. C., W. J. Plant, and G. R. Valenzuela (1986), Observation of breaking ocean waves with coherent microwave radar, in *Wave Dynamics and Radio Probing of the Sea Surface*, edited by O. M. Phillips and K. Hasselmann, pp. 285–293, Springer, New York.

Komar, P. D. (1998), *Beach Processes and Sedimentation*, 2nd ed., Prentice-Hall, Upper Saddle River, N. J.

Lee, P. H. Y., J. D. Barter, K. L. Beach, C. L. Hindman, B. M. Lake, H. Rungaldier, J. C. Shelton, A. B. Williams, R. Yee, and H. C. Yuen (1995), X band microwave backscattering from ocean waves, *J. Geophys. Res.*, *100*, 2591–2611.

Lee, P. H. Y., J. D. Barter, K. L. Beach, B. M. Lake, H. Rungaldier, H. R. Thompson Jr., L. Wang, and R. Yee (1999), What are the mechanisms for non-Bragg scattering from water wave surfaces?, *Radio Sci.*, *34*, 123–138.

Lewis, B. L., and I. D. Olin (1980), Experimental study and theoretical model of high resolution radar backscatter from the sea, *Radio Sci.*, *15*, 815–828.

Lippmann, T. C., and R. A. Holman (1990), The spatial and temporal variability of sand-bar morphology, *J. Geophys. Res.*, *95*, 11,575–11,590.

Liu, Y., S. J. Frasier, and R. E. McIntosh (1998), Measurement and classification of low-grazing-angle radar sea spikes, *IEEE Trans. Antennas Propag.*, *46*, 27–40.

McGregor, J. A., E. M. Poulter, and M. J. Smith (1997), Ocean surface currents obtained from microwave sea-echo Doppler spectra, *J. Geophys. Res.*, *102*, 25,227–25,236.

McGregor, J. A., E. M. Poulter, and M. J. Smith (1998), S band Doppler radar measurements of bathymetry, wave energy fluxes, and dissipation across an offshore bar, *J. Geophys. Res.*, *103*, 18,779–18,789.

McIntosh, R. E., S. J. Frasier, and J. B. Mead (1995), FOPAIR: A Focused Phased Array Imaging Radar for ocean remote sensing, *IEEE Trans. Geosci. Remote Sens.*, *33*(1), 115–124.

Miller, K. S., and M. M. Rochwarger (1972), A covariance approach to spectral moment estimation, *IEEE Trans. Inf. Theory*, *18*(5), 588–596.

Moller, D., S. J. Frasier, D. L. Porter, and R. E. McIntosh (1998), Radar-derived interferometric surface currents and their relationship to subsurface current structure, *J. Geophys. Res.*, *103*, 12,839–12,852.

Plant, W. J. (1990), Bragg scattering of electromagnetic waves from the air/sea interface, in *Surface Waves and Fluxes*, vol. 2, edited by G. L. Geernaert and W. J. Plant, chap. 11, pp. 41–108, Springer, New York.

Plant, W. J., E. A. Terray, R. A. J. Petitt, and W. C. Keller (1994), The dependence of microwave backscatter from the sea on illuminated area: Correlation times and lengths, *J. Geophys. Res.*, *99*, 9705–9723.

Puleo, J. A., G. Farquharson, S. J. Frasier, and K. T. Holland (2003), Comparison of optical and radar measurements of surf and swash zone velocity fields, *J. Geophys. Res.*, *108*(C3), 3100, doi:10.1029/2002JC001483.

Raubenheimer, B. (2002), Observations and predictions of fluid velocities in the surf and swash zones, *J. Geophys. Res.*, *107*(C11), 3190, doi:10.1029/2001JC001264.

Raubenheimer, B., R. T. Guza, and S. Elgar (1996), Wave transformations across the inner surf zone, *J. Geophys. Res.*, *101*, 25,589–25,597.

Schmidt, W. E., B. T. Woodward, K. S. Millikan, R. T. Guza, B. Raubenheimer, and S. Elgar (2003), A GPS-tracked surfzone drifter, *J. Atmos. Oceanic Technol.*, *20*, 1069–1075.

Sletten, M. A., J. C. West, X. Liu, and J. H. Duncan (2003), Radar investigations of breaking water waves at low grazing angles with simultaneous high-speed optical imagery, *Radio Sci.*, *38*(6), 1110, doi:10.1029/2002RS002716.

Smith, J. A. (1993), Performance of a horizontally scanning Doppler sonar near shore, *J. Atmos. Oceanic Technol.*, *10*, 752–763.

Smith, J. A., and J. L. Largier (1995), Observations of nearshore circulation: Rip currents, *J. Geophys. Res.*, *100*, 10,967–10,975.

Suhayda, J. N., and N. R. Pettigrew (1977), Observations of wave height and wave celerity in the surf zone, *J. Geophys. Res.*, *82*, 1419–1424.

Thornton, E. B., and R. T. Guza (1982), Energy saturation and phase speeds measured on a natural beach, *J. Geophys. Res.*, *87*, 9499–9508.

Trizna, D. B. (2001), Errors in bathymetric retrievals using linear dispersion in 3-D FFT analysis of marine radar ocean wave imagery, *IEEE Trans. Geosci. Remote Sens.*, *39*(11), 2465–2469.

Valenzuela, G. R. (1968), Scattering of electromagnetic waves from a tilted slightly rough surface, *Radio Sci.*, *3*, 1057–1066.

Wetzel, L. B. (1990), Electromagnetic scattering from the sea at low grazing angles, in *Surface Waves and Fluxes*, vol. 2, edited by G. L. Geernaert and W. J. Plant, chap. 12, pp. 109–171, Springer, New York.

Wright, J. W. (1968), A new model for sea clutter, *IEEE Trans. Antennas Propag.*, *16*, 217–223.

Young, I. R., W. Rosenthal, and F. Ziemer (1985), A three-dimensional analysis of marine radar images for the determination of ocean wave directionality and surface currents, *J. Geophys. Res.*, *90*, 1049–1059.

————————

S. Elgar and B. Raubenheimer, Woods Hole Oceanographic Institution, Woods Hole, MA 02543, USA. (elgar@whoi.edu; braubenheimer@whoi.edu)

G. Farquharson, EOL, NCAR, 3450 Mitchell Lane, Building 1, Boulder, CO 80301, USA. (gordon@mirsl.ecs.umass.edu)

S. J. Frasier, Microwave Remote Sensing Laboratory, Department of Electrical and Computer Engineering, University of Massachusetts, Amherst, MA 01003, USA. (frasier@mirsl.ecs.umass.edu)